Taylor & Francis
Taylor & Francis Group

Canadian Journal of Remote Sensing
Journal canadien de télédétection

ISSN: 0703-8992 (Print) 1712-7971 (Online) Journal homepage: https://www.tandfonline.com/loi/ujrs20

Multisensor and Multispectral LiDAR Characterization and Classification of a Forest Environment

Christopher Hopkinson, Laura Chasmer, Chris Gynan, Craig Mahoney & Michael Sitar

To cite this article: Christopher Hopkinson, Laura Chasmer, Chris Gynan, Craig Mahoney & Michael Sitar (2016) Multisensor and Multispectral LiDAR Characterization and Classification of a Forest Environment, Canadian Journal of Remote Sensing, 42:5, 501-520, DOI: 10.1080/07038992.2016.1196584

To link to this article: https://doi.org/10.1080/07038992.2016.1196584

Published online: 15 Jul 2016.

Canadian Journal of Remote Sensing, 42:501–520, 2016
Published with license by Taylor & Francis
ISSN: 0703-8992 print / 1712-7971 online
DOI: 10.1080/07038992.2016.1196584

Taylor & Francis
Taylor & Francis Group

Multisensor and Multispectral LiDAR Characterization and Classification of a Forest Environment

Christopher Hopkinson[1,*], Laura Chasmer[1], Chris Gynan[2], Craig Mahoney[1], and Michael Sitar[3]

[1]*Department of Geography, University of Lethbridge, 4401 University Drive, Lethbridge, Alberta T1K 3M4, Canada*
[2]*Silv Econ, 913 Southwind Ct., Newmarket, Ontario L3Y 6J1, Canada*
[3]*Teledyne Optech, 300 Interchange Way, Vaughan, Ontario L4K 5Z8, Canada*

Abstract. Airborne LiDAR is increasingly used in forest carbon, ecosystem, and resource monitoring. For practical design and manufacture reasons, the 1064 nm near-infrared (NIR) wavelength has been the most commonly adopted, and most literature in this field represents sampling characteristics in this wavelength. However, due to eye-safety and application-specific needs, other common wavelengths are 1550 nm and 532 nm. All provide canopy structure reconstructions that can be integrated or compared through space and time but the consistency or complementarity of 3D airborne LiDAR data sampled at multiple wavelengths is poorly understood. Here, we report on multispectral LiDAR missions carried out in 2013 and 2015 over a managed forest research site. The 1st used 3 independent sensors, and the 2nd used a single sensor carrying 3 lasers. The experiment revealed differences in proportions of returns at ground level, vertical foliage distributions, and gap probability across wavelengths. Canopy attenuation was greatest at 532 nm, presumably due to leaf tissue absorption. Relative to 1064 nm, foliage was undersampled at midheight percentiles at 1550 nm and 532 nm. Multisensor data demonstrated differences in foliage characterization due to combined influences of wavelength and acquisition configuration. Single-sensor multispectral data were more stable but demonstrated clear wavelength-dependent variation that could be exploited in intensity-based land cover classification without the aid of 3D derivatives. This work sets the stage for improvements in land surface classification and vertical foliage partitioning through the integration of active spectral and structural laser return information.

Résumé. Le LiDAR aéroporté est de plus en plus utilisé pour le suivi du carbone, des écosystèmes et des ressources forestières. Pour des raisons pratiques de conception et de fabrication, la longueur d'onde de 1064 nm dans le proche infrarouge a été la plus communément adoptée, et la plupart des études dans ce domaine représentent les caractéristiques d'échantillonnage dans cette longueur d'onde. Toutefois, en raison des besoins en matière de sécurité oculaire et d'applications spécifiques, d'autres longueurs d'onde communes sont 1550 nm et 532 nm. Toutes ces longueurs d'onde fournissent des reconstructions de la structure de la canopée qui peuvent être intégrées ou comparées dans l'espace et le temps, mais la cohérence ou la complémentarité des données LiDAR aéroportées en 3D qui sont échantillonnées à plusieurs longueurs d'onde est mal comprise. Nous décrivons ici les missions LiDARs multispectrales réalisées en 2013 et 2015 sur un site de recherche d'une forêt aménagée. La 1st a utilisé 3 capteurs indépendants, tandis que le 2nd a utilisé un seul capteur avec 3 lasers. L'expérience a révélé des différences entre les longueurs d'onde dans les fractions de retours au niveau du sol, dans les distributions verticales de feuillage ainsi que dans la probabilité de trous. L'atténuation de la canopée fut la plus grande à 532 nm, probablement en raison de l'absorption du tissu foliaire. Par rapport à 1064 nm, le feuillage a été sous-échantillonné aux percentiles à mi-hauteur à 1550 nm et 532 nm. Les données multicapteurs ont montré des différences dans la caractérisation du feuillage en raison des influences combinées de la longueur d'onde et de la configuration d'acquisition. Les données multispectrales à partir d'un unique capteur étaient plus stables, mais ont démontré une variation qui était clairement dépendante de la longueur d'onde qui pourrait être exploitée dans la classification de la couverture terrestre basée sur l'intensité sans l'aide de dérivés en 3D. Ce travail ouvre la voie à des améliorations dans la classification de la couverture terrestre et le partitionnement vertical du feuillage grâce à l'intégration de l'information spectrale et structurale de retours laser spectraux.

INTRODUCTION

Airborne light detection and ranging (LiDAR) point clouds and derivatives covering large areas are becoming increasingly available, either as commercial or open datasets, and offer great potential for high-resolution mapping at regional and national scales (e.g., Elberink et al. 2013). Aside from obvious benefits associated with high-accuracy digital elevation models (DEMs), these data are valuable in supporting a range of forest map-

Received 16 October 2015. Accepted 28 January 2016.

*Corresponding author e-mail: c.hopkinson@uleth.ca.

ping objectives (Nelson et al. 1984; Nelson 2013). In particular, the retrieval of the following vegetation parameters has been demonstrated: canopy height (Dubayah and Drake 2000; Means et al. 2000; Lefsky et al. 2002), canopy cover indices (Lefsky et al. 1999; Hopkinson et al. 2009), stand volumes, biomass, basal area, leaf area index (LAI), and diameter at breast height (DBH; Lefsky et al. 1999; Means et al. 1999; Naesset 2002; Clark et al. 2004; Patenaude et al. 2004; St-Onge, et al. 2008; Ni-Meister et al. 2010; Rosette et al. 2011). Recent efforts are moving toward the operationalization of LiDAR forest applications. For example, baseline forest resource inventory (FRI) (Woods et al. 2011), sample-based calibration of regional forest biomass products (Hopkinson et al. 2011; Wulder et al. 2012) and growth and yield monitoring, using LiDAR data, (Yu et al. 2004; Hopkinson et al. 2008; McRoberts et al. 2015) and possible extension from aerial photograph/LiDAR combinations (St-Onge et al. 2004). However, during the last 2 decades of LiDAR hardware development, there have been many technical advances, which have resulted in increased system accuracy, performance, capability, and specialization toward niche applications. Meanwhile, it has been highlighted that when data are collected through time, across space, or with different sensor sampling parameters, the consistency of the data and derivative forest attributes are not assured (Holmgren 2003; Hopkinson 2007; Hopkinson et al. 2008; Naesse2009; Stoker et al. 2014). As LiDAR monitoring of forest and other land surface attributes becomes operational, it is important to understand how modern LiDAR sensors differ in their characterization of terrain and overlying vegetated surfaces.

To date, much work on airborne LiDAR canopy data compatibility has focused on sensor configuration or sampling influences such as laser pulse power, footprint size, survey altitude, scan angle, or point density (e.g. Holmgren et al. 2003; Hopkinson 2007; Lim et al. 2008; Naesset 2009; Montaghi 2013). Historically, a focus on these configuration elements has been justified because they directly influence the sampling geometry and return signal detection. Moreover, the dominant wavelength of commercial airborne LiDAR sensors has tended to be 1064 nm due to raw material costs, diode reliability, optimal surface reflectance attributes, and eye-safety concerns. In recent years, however, we have witnessed a move toward more specialized wavelengths other than 1064 nm, such as 1550 nm due to the water absorption properties of this wavelength being safer for the eye at higher pulse powers, or 532 nm, where visible wavelengths are desired to simultaneously sample terrain, canopy, and bathymetric surfaces in open water and riparian areas. As airborne LiDAR systems of different wavelength have proliferated and the datasets collected are entered into a growing global database of point clouds, there is a need to directly compare the point cloud representations of canopy environments when sampled at different wavelengths.

Meanwhile, multichannel LiDAR sensors (e.g., the Titan)[1] are now available that combine multiple lasers to simultaneously actively sample and map terrestrial environments at multiple wavelengths. Multiwavelength airborne LiDAR is not new, as bathymetric systems such as Optech's Shoals or AHAB's HawkEye have incorporated dual wavelength LiDAR emission and multiple wavelength backscatter sampling since the late 1990s (Irish and Lillycrop 1999). However, employing active airborne multispectral LiDAR technologies in terrestrial forested environments is new and opens many research and application possibilities in terms of forest health and species classification, habitat mapping, and biomass and carbon stocks assessment (Morsdorf et al. 2009; Woodhouse et al. 2011; Hancock et al. 2012; Wallace et al. 2012).

Within a forestry context, the availability of commercial multispectral LiDAR enables the simultaneous observation of both structural and reflectance properties, which offers the potential to separate woody and leafy canopy elements from nonfoliage; or even the generation of passive image-based analogues such as normalized difference vegetation indices (NDVI) (Morsdorf et al. 2009; Wallace et al. 2012). This potential exists because reflectance spectra of vegetation contain information on plant pigment concentrations, leaf cellular structure, and leaf moisture content (Colwell 1974; Goetz et al. 1983). Leaves absorb visible light (~400 nm to 700 nm) efficiently, because these wavelengths are used in photosynthesis (Gates 1970; Knipling 1970). In the visible range, the maximum reflectance of a healthy green leaf is between 10% and 20% (Satterwhite and Henley 1990). In the near-infrared (NIR) range (~700 nm to 1300 nm), absorption drops to between 3% and 5%, and leaf-level reflectance is high, with about 40% to 60% of incident light scattered upward and the remainder transmitted or scattered downward (Satterwhite and Henley 1990). However, in the infrared (IR) spectrum (beyond ~1300 nm), absorption is typically between 30% and 50%, due to water within the canopy foliage (Knipling 1970; Satterwhite and Henley 1990).

An advantage of airborne LiDAR over passive imaging systems is that reflections (returns) from canopy and ground surfaces can be separated due to their morphological and geometric contexts (Axelsson 1999). However, different laser wavelengths will interact with the ground surface differently, and this has 2 important consequences: (*i*) for a given wavelength, if the ground surface has characteristics that absorb, or if the canopy preferentially occludes incoming energy, then the ability for LiDAR to accurately map subcanopy terrain could vary; (*ii*) given that soil and ground covers might reflect differently at different wavelengths, then multispectral LiDAR offers the potential for land surface and land cover classification in open and canopy covered environments (Yan et al. 2015). For example, a typical loam soil has an approximate reflectance of 28%, 40%, and 49% for visible, NIR, and IR radiation, respectively (Satterwhite and Henley 1990), which suggests that longer laser wavelengths might respond favorably over such surfaces as they experience lower absorption. However, it is also known that reflectance will vary with moisture content and that the IR wavelengths will be most susceptible to increased absorption with increasing moisture content (Lobell and Asner 2002).

[1]Teledyne Optech, Toronto, Canada

LiDAR-based land cover classification is not new (Yan et al. 2015). The 3D attributes of discrete-return single frequency LiDAR have been used to classify open water and wetland surfaces (Hogg and Todd 2007; Goodale et al. 2007; Crasto et al. 2015); forested land cover types and species (Moffiet et al. 2005; Antonarakis et al. 2008; Vaukonen et al. 2010; Korpela et al. 2010). LiDAR 3D derivatives have also been combined with passive multispectral data in forest environment classifications (Koukoulas and Blackburn 2005; Holmgren et al. 2008; Ke et al. 2010; Millard and Richardson 2013; Yang et al. 2014). Traditionally, however, single-frequency LiDAR signal intensity alone (i.e., through intensity thresholding) has not been considered of high value for species classification due to the many controls, in addition to surface reflectance, that influence intensity values (Moffiet et al. 2005; Hopkinson 2007). When 3D and intensity responses are considered together, forest species classification improves (Korpela et al. 2010). With multispectral LiDAR sampling of forest canopy and terrain surfaces, the complementary information contained in multiple intensity channels should alone facilitate improved land cover and perhaps species classification.

OBJECTIVE

This study aims to compare simple terrain and forest canopy attributes derived from each wavelength of 2 multispectral LiDAR datasets to assess whether the spatial and vertical information content in each channel differs. The 1st multispectral dataset compares data from 3 sensors to evaluate sensor-specific variations in terrain and canopy characterization, whereas the 2nd dataset is from a single 3-channel sensor to quantify whether data from multiple channels are complementary or redundant. Tests are performed primarily at forest stand scale to place the analysis in a forest resource inventory context. Finally, the work explores the possibility of combining the multispectral LiDAR data alone in standard image-based classifications of major land cover types in the study area.

DATA AND METHODS

Study Area

The study was conducted in the North Tract of the York Regional Forest, 50 km north of Toronto, Canada, on the Oak Ridges Moraine (Figure 1). Almost 80% of the Tract is coniferous plantations, with some considered to be among the oldest in southern Ontario. The deep sands that cover the site support a diversity of over 40 tree species with a dominance of white pine (*Pinus* strobus) and sugar maple (*Acer saccharum)*. Much of the original forest was cleared for agriculture in the mid to late 1800s, however, the infertile soils could not sustain this practice. Beginning in 1924, forest cover was completely restored by planting coniferous seedlings on abandoned agricultural lands.

This area was chosen because it has been the subject of ongoing LiDAR research since 2000 and is easily accessible through a network of recreational trails. The York Regional Forest research site was initially set up by the authors due to its proximity to the airborne laser terrain mapper (ALTM)[2] sensor testing and calibration site. Consequently, acquiring repeat LiDAR datasets over the study area could be achieved with relative ease during optimal conditions or when new systems were being tested. The study site has been the focus of several LiDAR forest studies (Hopkinson et al. 2004; Chasmer et al. 2006; Hopkinson et al. 2008; Lim et al. 2008) and in addition to the York Region Forest Resource Inventory (FRI), several field plots have been established within the North Tract to provide a means of plot-level model calibration.

The FRI stand polygons used in this analysis are presented in Figure 1. These 41 stands have been chosen because they fall within the overlap region of the 4 multispectral LiDAR sets described following. Within this selection of stands, the ages range from approximately 10 to 70 years of growth within structurally complex hardwood and mixed regeneration stands to uniform conifer plantations, each undergoing a range of treatments. Consequently, althoughh this is a largely managed forest environment, it represents a diverse sample set of canopy conditions over a relatively small area.

Data Collection

Four airborne LiDAR datasets collected from 4 different sensors over 3 flight missions were used for this multisensor, multispectral study. In the summer of 2013, 2 airborne data collections were conducted 1 month apart during dry conditions at peak foliage conditions. The 1st flight in late July deployed Aquarius (532 nm) and Orion (1550 nm) sensors co-mounted in a Piper Chieftan survey aircraft. The 2nd flight in late August deployed a Gemini (1064 nm) sensor. In July of 2015, a 3rd flight was carried out over an overlapping but coincident area of interest (AOI) with a Titan sensor that simultaneously captured the same 3 wavelengths as did the earlier multisensor missions. All 4 sensors[3] utilize equivalent pulse detection and ranging procedures, including the capture of up to 4 returns from a single emission, each scaled according to its peak pulse amplitude (referred to as return "intensity").

The sensor and survey settings for all 4 datasets are provided in Table 1. Efforts were made to maintain a constant survey configuration with a ground speed of 135 knots, flight line side-lap of 50%, and altitude of 1 km for all flights, but air traffic control at the nearby Pearson International Airport imposed some minor deviations. Consequently, the July 2013 flight was ∼100 m lower and the July 2015 flight ∼70 m higher than the planned 1km survey altitude. All other

[2]Teledyne Optech Inc., Toronto, Ontario, Canada
[3]Manufactured by Teledyne Optech, Toronto, Canada

FIG. 1. Study area including forest inventory polygons (white) and field plot locations (yellow). Image is a 3-band (532 nm, 1064 nm, 1550 nm) composite image of the Titan airborne lidar data. Inset: Map of Canada showing location of the study site.

important sensor settings were typical for the sensors, survey altitude and the nature of the ground surface being mapped (Table 1). The diversity in sensor attributes represents the typical range of commercial airborne LiDAR mapping sensors and is therefore ideally suited to the dual objective of evaluating the consistency of terrain and canopy attributes and the influence of different sampling wavelengths.

The sensors demonstrated some variation in pulse repetition frequency (PRF) and beam divergence, and this was due to the different hardware set up and typical usage of each sensor. For example, the Aquarius sensor is a combined topographic and bathymetric system requiring operation in the visible portion of the spectrum. Given that a 532-nm laser pulse is not eye safe at equivalent operating power levels to the Orion (1550 nm) and Gemini (1064 nm) wavelengths, some compromise on PRF and beam divergence is unavoidable; i.e., pulses are spaced more in time and the beam is widened to reduce the energy concentration within the footprint (for an explanation of the pulse power to beam divergence relationship see Hopkinson 2007). The main result of these configuration differences is a range in ground level sampling density from 1.4 pts m-$^{-2-}$ to 2.7 pts m^{-2} in the 2013 multisensor dataset (Table 1). A higher sampling density was not practical with the Aquarius sensor due to the constraints imposed by survey altitude. The high-density

TABLE 1
LiDAR sensor configuration and survey settings for each ALTM system

Parameters	Sensor or Mission Values					
Sensor model	Aquarius	Gemini	Orion C		Titan	
Date	22/07/13	24/08/13	22/07/13		02/07/15	
Wavelength (nm)	532	1064	1550	532	1064	1550
PRF (kHz)	50	70	125	100	100	100
Pulse width (ns)	8	12	2.6		n/a	
Pulse energy (μJ)	70	97	18		n/a	
Peak pulse power (kW)	8.8	8.1	6.9		n/a	
Divergence (1/e) (mRad)	0.7	0.25	0.22	0.7	0.25	0.22
Receiver aperture diameter (m)	0.05	0.05	0.05		0.075	
FOV (deg)	30	40	30		30	
Altitude (km agl)	0.9	1	0.9		1.07	
Emission sample density (pts m^{-2})	1.5	1.4	2.7	3	3	3
Footprint area (m^2)	0.31	0.05	0.03	0.44	0.06	0.04
Intensity range (bits)*	12	12	12		12	

*Intensity units are undefined and represent a scaled index of the peak mV reading observed at the sensor receiver. A 12-bit scale equates to a range of 0 to 4,096 integer increments.
n/a: values are not available for publication.

sampling of the Orion C is typical of the low-altitude design criteria of the sensor, however, the Gemini has a much higher altitudinal range. Consequently, the Orion was operating near its upper altitude and lower PRF limits, while the Gemini was nearer to its typical lower altitude and upper PRF limits. The Titan is the most modern of the sensors, with greater PRF capabilities than any of the others. However, it was operated at 100 kHz / channel (or 300 kHz overall) to produce data that would be as comparable as possible given different hardware design and operational constraints.

To supplement the available FRI data, a field visit was carried out between July 7 and 10, 2015, to survey land cover types (forest stand and crop type, and open area coverages of sand, gravel, and asphalt) within the study area. In addition, 8 differential GPS-surveyed forest mensuration plots were established to determine species mix, basal area, and to collect 40 (5 per plot) digital hemispheric photographs (DHPs).

Comparative Analysis

Raw sensor point clouds were constructed for each flight line using proprietary data integration routines (Teledyne Optech, Canada), while subsequent point cloud and raster analyses were carried out using Terrascan (Terrasolid, Finland), LAStools (rapidlasso GmbH, Germany), Surfer (Golden Software, USA), ArcGIS (ESRI, USA), and Geomatica (PCI, Canada). To evaluate the general LiDAR signal return properties across the study area, the signal intensities of all returns were averaged across a 20 m $\times$ 20 m grid within LAStools and compared. Following ground classification (Axellson 1999), a 1-m resolution digital elevation model (DEM) of the terrain was gridded for each wavelength dataset using the triangulation interpolation routine in Surfer. Canopy height normalization was carried out using the ground classified data, so that point-cloud-based foliage profile and gap probability estimates could be generated for each wavelength dataset and compared.

As an index of the cumulative foliage profile, height percentiles were extracted and aggregated to a 20 m grid using the LAScanopy module within LAStools for percentile (%) increments (PXX) ranging from P00 (minimum or ground reference) to P100 (maximum or canopy top), with several increments between (P01, P05, P10, P25, P50, P75, P90, P95, P99). The tails of the percentile distributions were sampled at higher frequency, because this is where most differences are likely to occur (Hopkinson 2007) and data were aggregated to a 20-m grid to facilitate direct comparison across wavelengths, while mitigating uncertainty due to slight differences in sampling density (Lim et al. 2008) or positional accuracy.

Two indices of gap probability (or 1 – fractional cover) were extracted across a 20-m grid, using LAScanopy. Although intensity-based approaches to gap probability (or fractional cover) have proven more closely related to absolute values of overhead canopy gap probability, point-cloud-ratio-based approaches tend to be accurate predictors, as long as suitable scaling factors are applied (Hopkinson and Chasmer 2009). Consequently, gap probability (P) indices were extracted from: (*i*) first and single returns only (P_{first}), as these represent the first encounter of an emitted pulse with foliage or terrain; and (*ii*) from all returns (P_{all}), as these represent a more complete terrain to canopy profile. In both cases, a height threshold of 2 m

was used to maximize the separation of understory and canopy elements:

$$P = \frac{\sum B}{\sum T} \quad [1]$$

where T = total number of returns within the full vertical profile and B = number of below canopy returns that are located beneath the specified height threshold.

Following construction of the gridded DEMs, foliage height statistics and gap probability indices were compared within each of the multiwavelength datasets in ArcGIS. Given the 2-year time period between the multisensor and Titan data collections, grid-to-grid comparisons were limited to the coincident multispectral datasets. Direct spatial comparisons were made across the AOI by subtracting the most typical LiDAR wavelength of 1064 nm from the 532 nm and 1550 nm grids to visually illustrate deviations. This visual analysis was applied to the 1-m DEM, the P99 height surface, and both P_{first} and P_{all} gap probability grids. P99 was chosen, because it represents a reliable index of grid-level maximum canopy height that is not susceptible to the influence of outliers. (Note: P100 is derived from the single highest point across a 20 m × 20 m grid, whereas P99 is a function of all points within the sample where the nominal minimum number of points in any grid will be >500). Gap probability was similarly compared in order to evaluate whether P estimates are stable across wavelengths. Canopy height profiles were stratified by wavelength and mature stand type (conifer, hardwood, and all stands including mixed wood), then compared graphically. Stand type designations were derived from the York Regional Forest FRI and for the purpose of this analysis, stands reporting >75% hardwood or conifer are assigned to that class, while stands reporting 50%–75% are designated mixed.

Multispectral Classifications

Several dominant land cover types were identified across the study area by using a combination of field survey and photographs, interpretation of high-resolution Google Earth imagery, and FRI stand attributes. Because the area surveyed in 2015 was larger than that of 2013, more land cover training sites could be included and there was higher confidence that field crops (corn and hay) were correctly identified in 2015. Overall, 8 discernible land cover types were identified in 2015 (asphalt, sand, gravel, corn, hay, pine/spruce, larch, and hardwood). Larch (*larix*) was singled out from the pine and spruce conifer class in 2015, because a stand on the north side of the 2015 AOI (just outside the 2013 AOI) contained a high proportion of larch trees and they were visibly more distinct than pine (*pinus*) or spruce (*picea*), which were the overall dominant conifer type. For the 2013 data, insufficient known training data were available for larch, corn, or gravel, so it was possible to attempt to classify only the remaining 5 land cover types.

The all-return point clouds of each intensity channel were gridded in LAStools in order to produce 1-m average intensity rasters, then imported into ArcGIS. Image speckle and blank grid nodes were removed using a majority filter prior to constructing 3-band composite images with 532 nm, 1064 nm, and 1550 nm as image channels 1, 2, and 3, respectively (Figure 1). The 2013 and 2015 intensity composites were imported into PCI Geomatica (Ottawa, Canada) to perform 3 typical image-based supervised classifications using the previously identified training areas. For simplicity and speed, minimum distance, maximum likelihood, and parallelepiped classification routines were tested, and the method deemed most successful based on confusion matrix results was chosen for subsequent comparison with stand FRI and field plot assessments of conifer vs. hardwood species. It is of note that the aim of these classifications is not ultimate accuracy, but to demonstrate the difference in the capabilities for classification purposes of the multisensor, multispectral vs. single-sensor, multispectral LiDAR datasets.

RESULTS

Signal Intensities

The average intensities of all returns across the study area are presented for each of the sensor wavelengths in Figure 2 (2013 multisensor) and Figure 3 (2015 Titan). The intensity values represent measures of peak return signal amplitude but are not radiometrically calibrated to standard units such as Jules (peak amplitude) or watts (integral of the response curve). All datasets produce intensity responses nearer the lower end of the 12-bit (0 – 4,096) scale. For the multisensor data, the Gemini 1064-nm wavelength demonstrates the highest levels and the greatest range in reflectance over this woodland environment. The mean Gemini 1064-nm intensity is >9 times greater than that from the Orion 1550-nm and >17 times greater than the Aquarius 532-nm (Figure 2). The distributions are closer for the 2015 Titan data (Figure 3), because ensuring compatible intensity response was a design consideration of this multichannel sensor. However, given that the Titan intensity channel responses do not represent surface reflectance, they cannot be used to construct spectral ratios or indices (e.g., NDVI) without normalization and calibration (Yan and Shaker 2015).

For all missions and wavelengths, the intensity distributions are bimodal, with the majority of returns clustered around the lower intensity peak. The lower intensity peaks are associated with forest covered areas whereas the higher intensity peaks generally represent areas of open fields and corridors where there is no canopy cover to split the emitted pulse into multiple returns. The one exception is in the center of the study area where high average intensity values in the 1064-nm and 1550-nm images (Figures 2b, 2c, 3b, and 3c) are associated with stands containing mostly hardwood (*Acer*) species. The elevated average intensity response observed for hardwood stands compared to the surrounding conifer canopies at 1064 nm is useful for forest stand type classification and has been observed by others (Orka et al. 2007; Orka et al. 2009; Korpela et al. 2010).

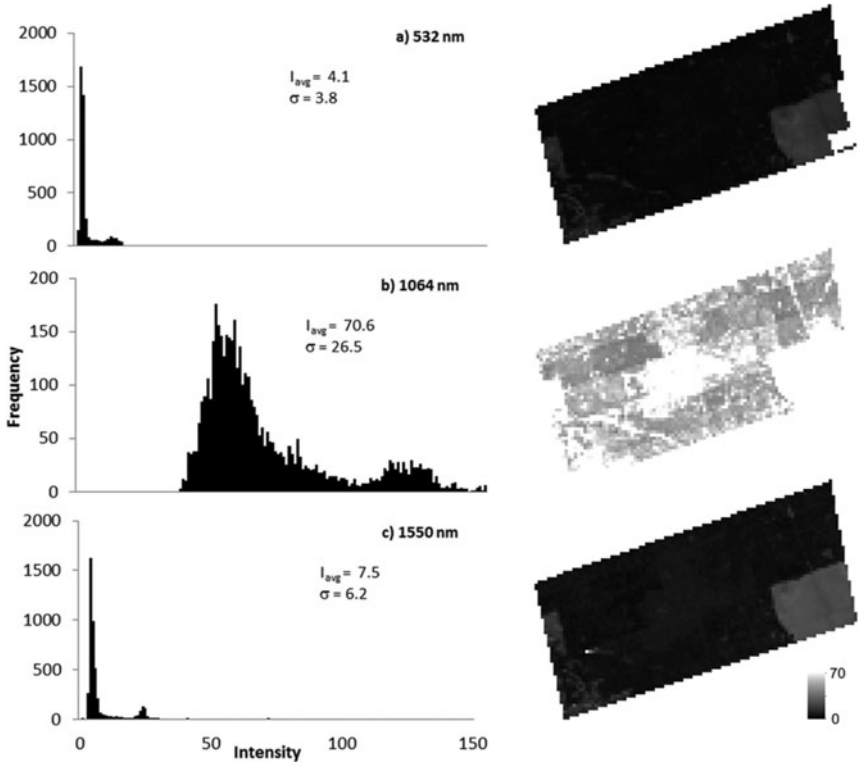

FIG. 2. Frequency distributions (left) and linearly-scaled images (right) of the all-return signal intensities for each of the 2013 mission datasets. The arbitrary intensity scale is kept constant both in the distributions (0–150 units) and the images (0–70 units) to allow direct comparison. The average and standard deviation of each intensity distribution is inset.

DEM and Canopy Height

Summary statistics for the DEM and P99 surface comparisons are provided in Table 2. The mean surface elevation offsets and standard deviations for multisensor and Titan mission data are close to the noise level typical within LiDAR data, which, in the absence of additional higher accuracy ground control, suggests that all 3 datasets have produced 1-m DEMs to a similar level of accuracy. P99 differences are only slightly larger than DEM surface offsets but are still close to noise levels. To discern notable wavelength-dependent behavior, we need to observe the surface raster differences. Note, the 12 cm decrease in mean ground elevation between the 1064 nm multisensor and Titan datasets might be due to using different base station controls or actual changes in the ground surface conditions between 2013 and 2015. However, the 48-cm increase in observed P99 during the same period is likely due to 2 years of canopy height growth, because this is commensurate with growth rates previously observed in this area (Hopkinson et al. 2008). In both cases, the wavelength-dependent offsets are not impacted by these temporal changes.

The 1064-nm baseline 1-m DEM and 20-m P99 canopy height grid across the study area are, respectively, presented for the multisensor and Titan missions in Figures 4 and 5, along with the comparative deviation surfaces for the 532-nm and 1550-nm surfaces. Variations in terrain height and morphology, as well as canopy height heterogeneity, are clearly evident across the study area (Figures 4a,d, 5a, and d). There is >30 m of terrain relief with canopy heights ranging from 0 m in clearings up to ∼30 m above ground surface in riparian areas and mature hardwood stands.

Differences in multisensor DEM surface elevation of up to ∼0.5 m are illustrated in Figure 4b and 4c for the 532-nm and 1550-nm wavelength datasets, respectively. It is noteworthy that the 532-nm surface is mostly above the 1064-nm DEM. Also, the visible differences and offset statistics indicate that the 532-nm DEM possesses the most noise, with small regions up to and exceeding 20 m across where the surface is >0.5 m above or below the 1064-nm DEM. Similar patterns and directional offsets are also observed for multichannel Titan DEM (Figure 5 and Table 2), but overall, the DEMs are more consistent across wavelengths than those obtained from different sensors.

The mean difference in multisensor-P99 canopy height grids between the 1064-nm and 532-nm datasets is −0.16 m (σ = 0.76, p <0.05). In addition, there are localized patterns of deviation, often associated with areas of lower DEM quality (Figure 4b), where the 532-nm P99 surface is several meters below the 1064-nm P99 grid. The mean 1550-nm P99 difference is +0.11 m (σ = 0.10, p <0.05), but individual regions of de-

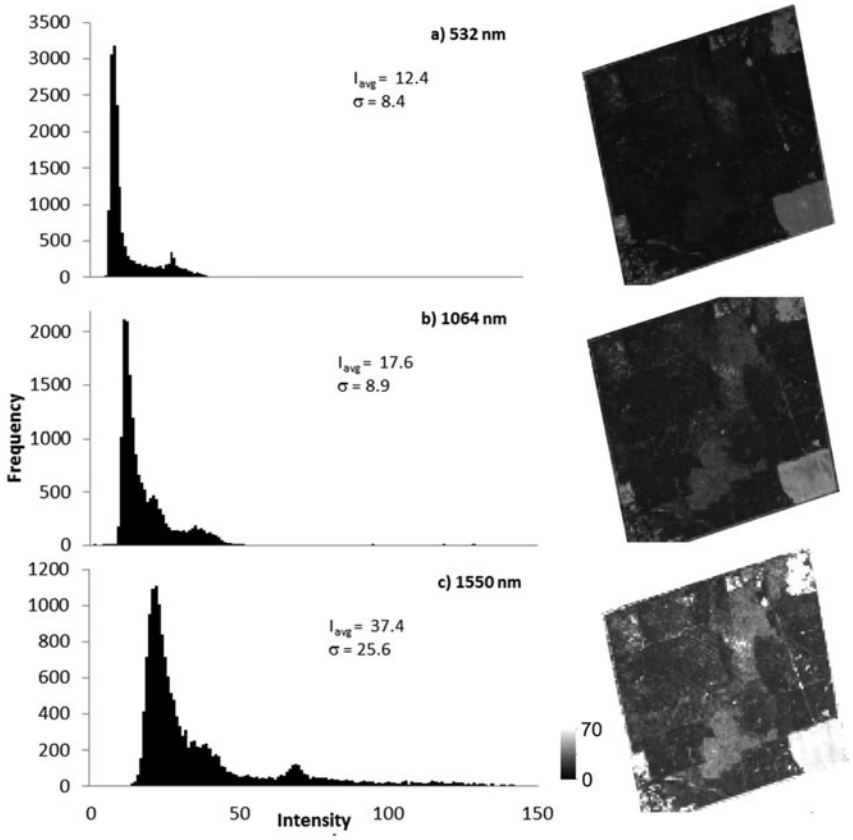

FIG. 3. Frequency distributions (left) and linearly-scaled images (right) of the all-return signal intensities for each channel of the 2015 Titan data set. The arbitrary intensity scale is kept constant both in the distributions (0–150 units) and the images (0–70 units) to allow direct comparison. The average and standard deviation of each intensity distribution is inset.

viation are smaller and associated with flight line noise. The corresponding Titan P99 comparisons illustrate smaller offsets that differ in sign to the multisensor mission (Table 2), although appearing to show no notable spatial patterns (Figures 5e and f) aside from minor linear feature edge artefacts. Overall, the P99 differences between 1064-nm and 1550-nm are minor and within noise levels, while at 532 nm, systematic differences are limited to the multisensor mission in areas of hardwood cover, where DEM errors are also enhanced. The poor upper canopy sampling of the Aquarius 532-nm dataset is likely due to the high proportion of visible light absorbed in photosynthesis (Gates 1970), combined with the low-intensity response of this particular sensor within this environment (Table 2).

Gap Probability

Summary statistics for gap probability (P_{first} and P_{all}) comparisons are provided in Table 3. Neither P_{first} nor P_{all} demonstrate any statistical difference at the 95% confidence level between corresponding multisensor or Titan estimates at 1064 nm, despite being captured 2 years apart. However, apart from the P_{first}

TABLE 2
Mean DEM and P99 height differences from 1064 nm within overlapping part of AOI

	DEM (m)		P99 (m)	
	Multisensor	Titan	Multisensor	Titan
1064	257.51 (5.63)	257.39 (5.46)	19.07 (7.67)	19.55 (7.78)
Δ 532	0.07 (0.18)	0.04 (0.20)	−0.16 (0.76)	0.12 (0.50)
Δ 1550	−0.02 (0.12)	−0.03 (0.08)	0.11 (0.42)	−0.03 (0.43)

Standard deviation in parentheses

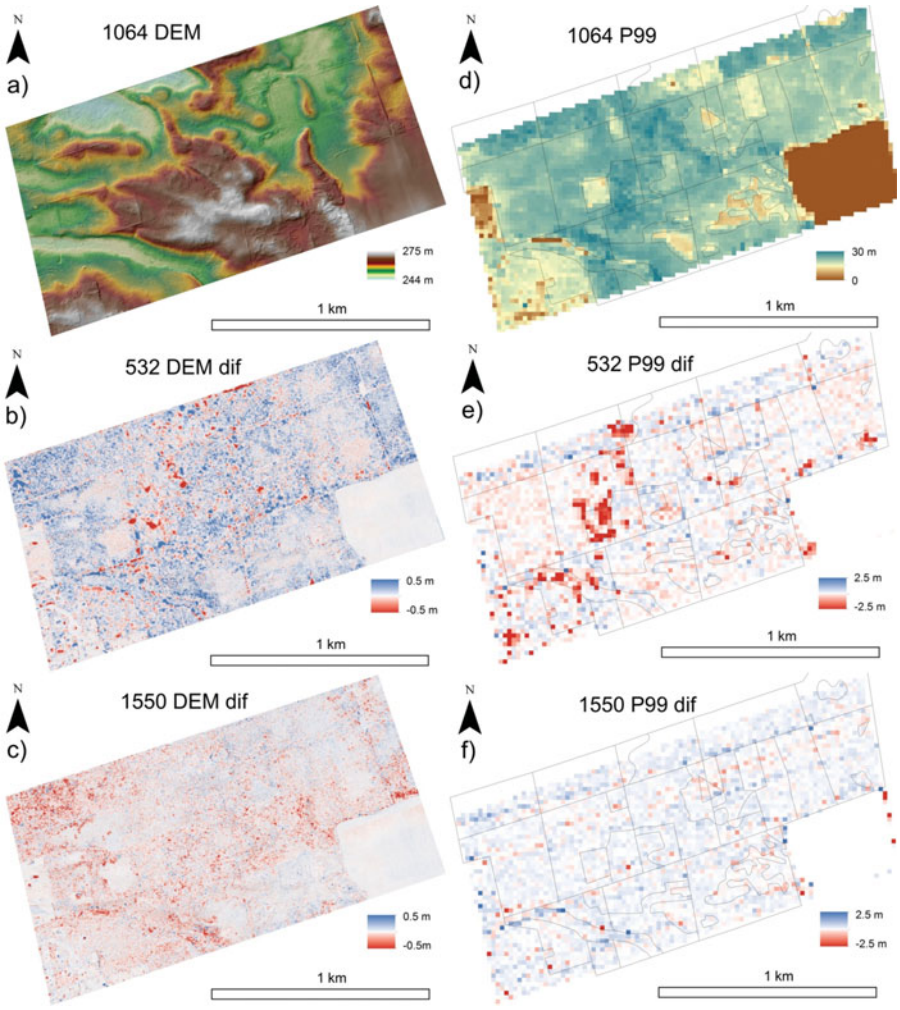

FIG. 4. a) 1064 nm 1 m DEM with differences illustrated for the 532 nm (b) and 1550 nm (c) DEMs of the 2013 multi-sensor campaign. d) 1064 nm P99 20 m × 20 m canopy height grid with differences illustrated for the 532 nm (e) and 1550 nm (f) P99 grids. Note: for plots b, c, d, and e, a positive difference (blue) indicates that the surface overlies that of the corresponding 1064 nm surface. FRI stand polygon outlines added to P99 maps.

1550-nm Titan estimate, all other 532-nm and 1550-nm P_{first} and P_{all} values do differ significantly from their corresponding 1064-nm gap probability. This demonstrates that a simple return ratio gap probability, whether based on all returns or first returns, will vary with laser wavelength.

It is a priori known that neither P_{first} nor P_{all} will provide a 1:1 estimate of true canopy gap probability (Hopkinson and Chasmer 2009), and this is illustrated in the comparison of field DHP results with spatially corresponding P_{first} and P_{all} estimates for each wavelength (Table 4). Only the Titan data are compared because the field data were captured within a week of the 2015 survey. From the 40 DHP images collected within 8 plots (Figure 1), the mean overhead (0°–10°) gap probability was found to be 21% (Min: 1%, Max: 6 7%, σ: 20%).

P_{all} and P_{first} for all wavelengths consistently underestimate gap probability (Table 4), with none of the results close to a 1:1 relationship with field DHP estimates. P_{all} produces improved estimates over P_{first} in terms of regression residuals, intercept, and scale factor. There are also marginally improved results for both models at 532 nm in terms of scale factor and intercept. This might be because 532 nm is a visible wavelength, as are DHP images, however, the differences in overall wavelength responses are negligible.

Spatially explicit multisensor gap probability results are presented in Figure 6. The upper canopy sampling tendency of first and single returns is evident in the small average 1064-nm P_{first} (Figure 6a, Table 3) of 19.9% with a high proportion of the study area illustrating a gap probability close to zero; i.e., dense canopy cover. In contrast, the more complete treatment of the full canopy profile is evident in the higher average P_{all} (Figure 6d, Table 3) of 32.9%, with spatial variations that show some correspondence to FRI polygons.

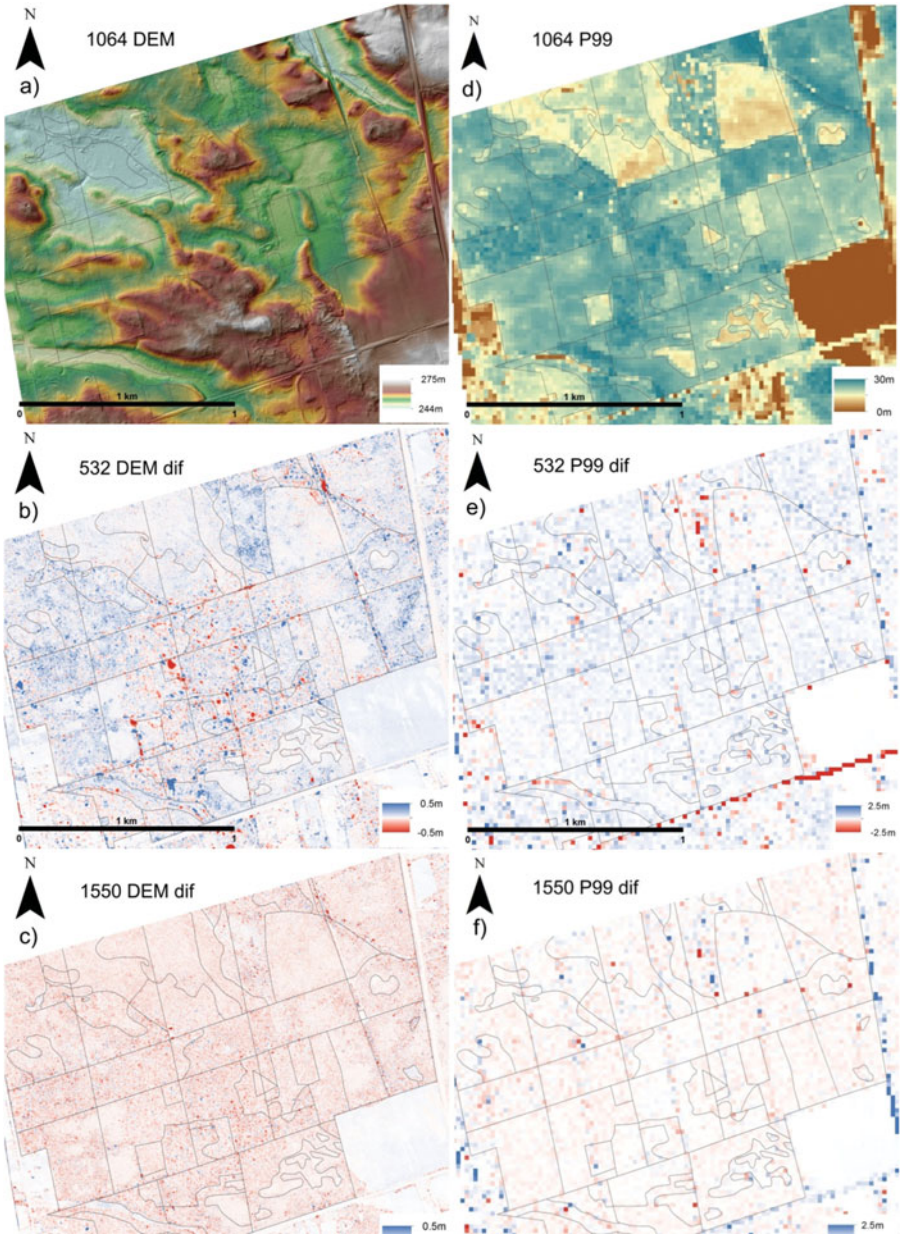

FIG. 5. a) 1064 nm 1 m DEM with differences illustrated for the 532 nm (b) and 1550 nm (c) DEMs of the 2015 Titan campaign. d) 1064 nm P99 20 m × 20 m canopy height grid with differences illustrated for the 532 nm (e) and 1550 nm (f) P99 grids.

Mean differences in multisensor gap probability by wavelength (Table 3) indicate that 532 nm and 1550 nm both produce overall higher values than 1064 nm for first returns (6.9% and 1.5% in Figure 6b and c, respectively) and lower values for all returns (1.2% and 4.2% in Figure 6e and f, respectively). For the 1550-nm P_{all} (Figure 6f), the difference is almost exclusively negative, with any visual patterns dominated by noise and scan line artifacts. (Note: Slight differences between datasets are expected to be elevated at the edge of flight lines, because this is where vertical sampling and point density are the least uniform.)

As the comparison between multisensor P_{first} and P_{all} demonstrates (Figure 6a and d), an increase in P indicates that a higher proportion of the point cloud exists below the 2-m height threshold. Therefore, the decreases in P_{all} observed for 532 nm and 1550 nm in Figure 6e and f indicate that higher proportions of all returns lie above the threshold than those for 1064 nm; i.e., the 1064-nm data demonstrate generally increased foliage penetration (canopy transmittance) and improved representation of the near-ground level.

Comparative gap probability results for the Titan are visually similar to the multisensor results at 1064 nm, in that P_{all} val-

TABLE 3
Mean gap probability for 1064 nm and 20 m grids and corresponding differences for 532 nm and 1550 nm channels within the overlapping multisensor and Titan mission AOI

	P_{first} (%)		P_{all} (%)	
	Multisensor	Titan	Multisensor	Titan
1064	19.9 (32.2)	19.3 (32.3)	32.9 (27.6)	25.9 (29.9)
Δ 532	6.9 (7.1)	2.7 (4.1)	−1.2 (6.4)	1.4 (3.8)
Δ 1550	1.5 (3.3)	0.1 (1.1)	−4.2 (3.9)	1.0 (1.3)

Standard deviation in brackets

TABLE 4
LiDAR gap probability (P) regressed against overhead (0 deg–10 deg) DHP gap fraction for 8 plots (40 DHP images) captured within a week of the 2015 mission

Wavelength	1550		1064		532	
Return ratio model	P_{all}	P_{first}	P_{all}	P_{first}	P_{all}	P_{first}
Average (%)	11	3	10	3	11	6
Range (%)	19	9	19	9	22	13
r^2	0.75	0.31	0.77	0.29	0.75	0.60
Scale factor	1.91	2.95	1.96	2.74	1.87	2.50
Y intercept (%)	0	12	0	13	0	7

ues are higher than P_{first} and with decreased gaps in the central hardwood stand area (Figure 7a and b). There is also a visual correspondence in the patterns of 532-nm gap probabilities for the multisensor and Titan missions (Figures 6b, 6e, 7b, and 7e). This indicates that much of the 532-nm vs. 1064-nm gap probability differences are systematically driven by wavelength and not merely sensor or mission configuration differences. Con-

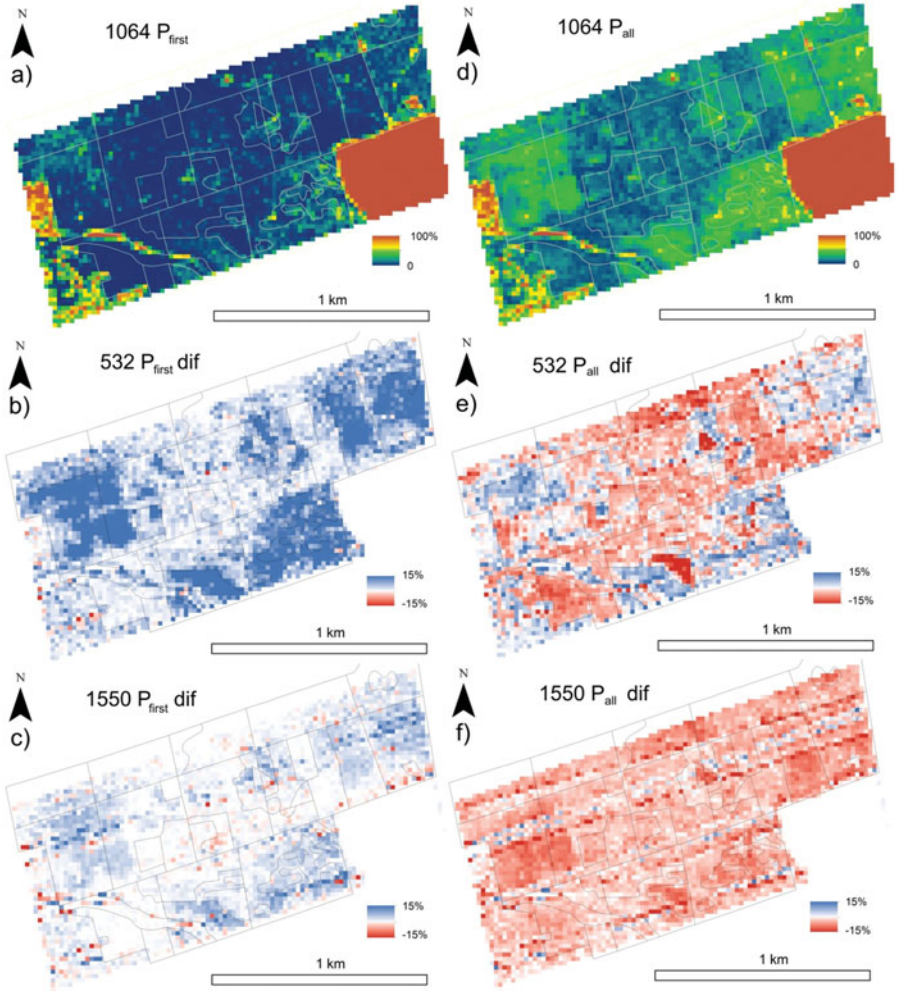

FIG. 6. a) 1064nm 20m × 20m raster grid of P_{first} with differences illustrated for 532nm (b) and 1550nm (c) for the 2013 multi-sensor mission. d) 1064nm 20m × 20m raster grid of P_{all} with differences illustrated for 532nm (e) and 1550nm (f). Note: a positive difference value (blue) indicates that the associated gap probabilities are greater than the 1064 nm grid.

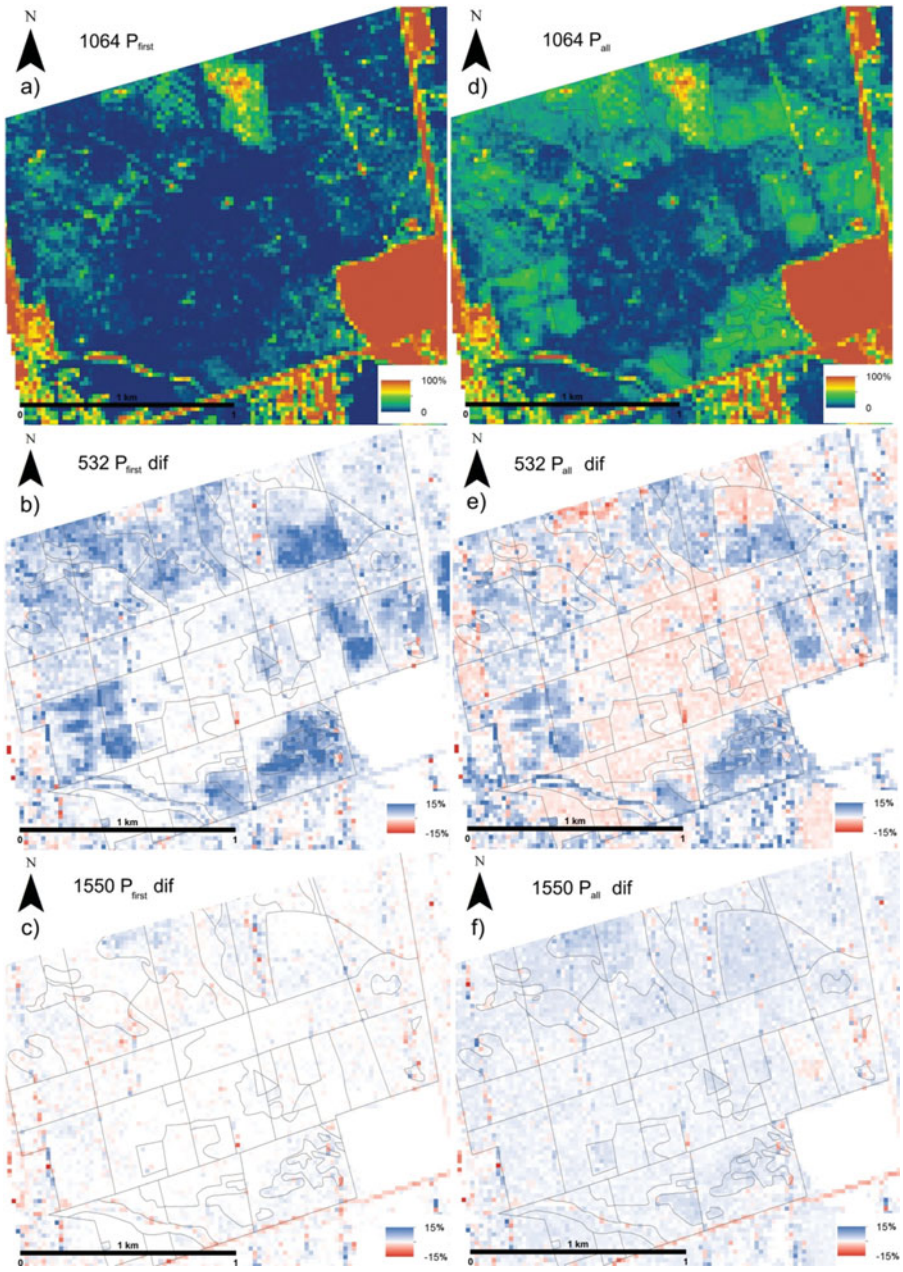

FIG. 7. a) 1064nm 20m × 20m raster grid of P_{first} with differences illustrated for 532nm (b) and 1550nm (c) for 2015 Titan mission. d) 1064nm 20m × 20m raster grid of P_{all} with differences illustrated for 532nm (e) and 1550nm (f).

versely, the 1550 nm to 1064 nm gap probability differences from the Titan mission (Figure 7 c and f) are smaller than those from the multisensor mission (Figure 6 c and f) while also being dominated by noise and scan line artifacts.

Height Percentiles by Stand Type

Pulse penetration and the differences in foliage profile representation by wavelength and by stand type are further elucidated in Figure 8. Canopy-to-ground percentile distributions have been aggregated and plotted for 3 mature stand classes containing (*i*) any species mix or (*ii*) >75% conifer or (*iii*) >75% hardwood within the study area. This represents ~50% sampling of the FRI stand population within the 2013 and 2015 AOIs. The 1064-nm foliage height cumulative distributions (Figure 8a and 8d) are significantly different (Kolmogorov–Smirnov test, $p < 0.01$), from all corresponding distributions (Figures 8b,c,e), aside from those produced from the 1550-nm channel in the Titan sensor (Figure 8f).

Although the mean maximum heights (P100) of mature conifer and hardwood stands are close at ~25 m for the 2013 and

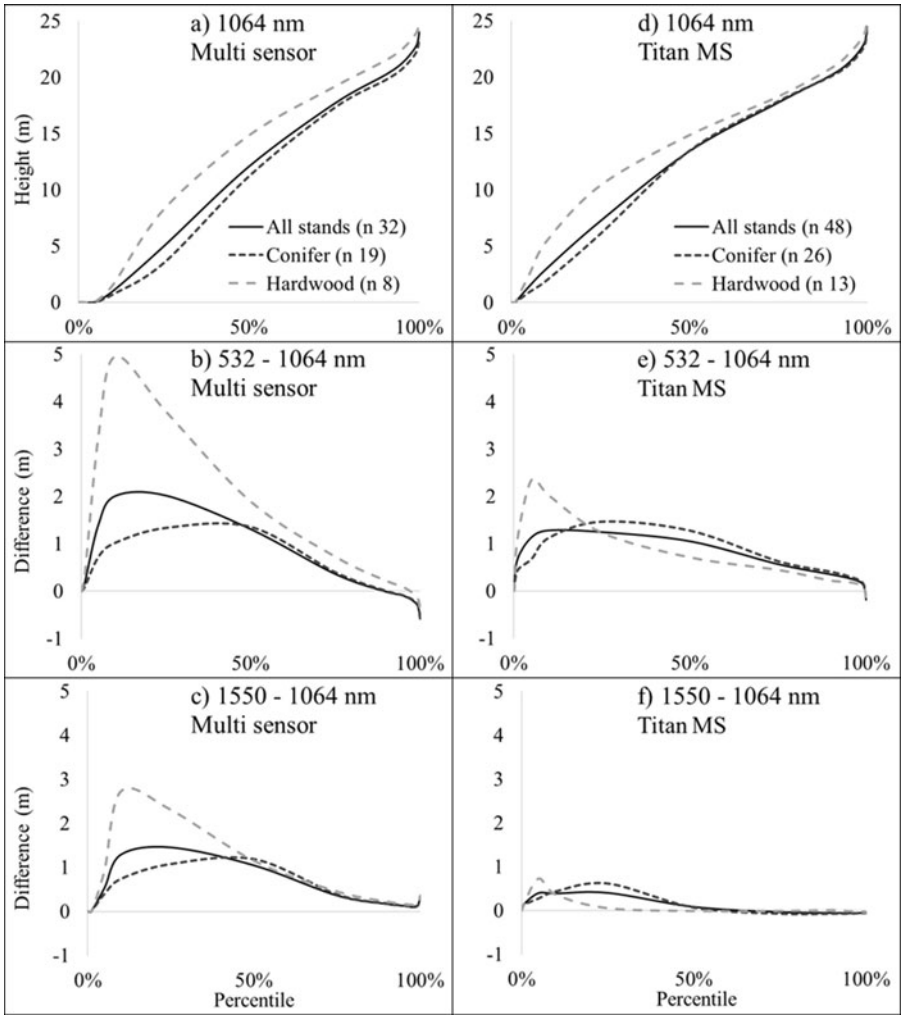

FIG. 8. Multi sensor 2013 and Titan 2015 mission height percentiles (x-axis) and wavelength dependent differences (y-axis) of all, conifer and hardwood stands. Stands chosen for study are all mature (> 20m in height). "All stands" contain either homogeneous or mixed species.

2015 missions, the foliage distributions are distinct with slightly greater deviations in the mid-percentile range (P25–P75). This upward "bulge" in the hardwoods is characteristic of increased foliage in a distinct overstory of tree crowns. By comparison, the more linear distribution displayed by the conifer plantations is characteristic of a higher stem density and deeper tree crown profile.

Common to the multisensor and Titan missions, the 1064-nm aggregated foliage profile for all stands (Figure 8a,d) tends to better represent the lower canopy heights relative to both 532 nm (Figure 8b,e) and 1550 nm (Figure 8c,f). Maximum differences occur at P25, where the multisensor 1064-nm profile is 1.9 m (Figure 8b) and 1.4 m (Figure 8c) below the corresponding 532-nm and 1550-nm profiles, respectively. Wavelength-dependent distribution deviations are greatest overall in the hardwood stands during the multisensor mission, where the 532-nm profile is ∼5 m above 1064 nm at P25. Meanwhile, and as observed in the P99 canopy height comparisons, there are significant differences (p <0.01) in the upper distribution tails of the multisensor data where the mean maximum of the 1064-nm profile (P100) is 0.34 m ($\sigma = 0.10$) below that for 1550 nm and 0.59 m ($\sigma = 0.56$) above that for 532 nm.

It is clear from the 2015 Titan data (Figure 8e,f), that some of the profile-based wavelength deviations between conifer and hardwood resemble the patterns observed in the 2013 multisensor mission (Figure 8 b,c). These similarities indicate that conifer and hardwood stands interact with laser pulses in distinct ways, depending on the wavelength of light being used. Given that the P25 to P75 heights appear greater for 532 nm and 1550 nm, this indicates that these wavelengths have preferentially sampled upper regions of the canopy. However, although similar patterns are evident in both missions, the Titan

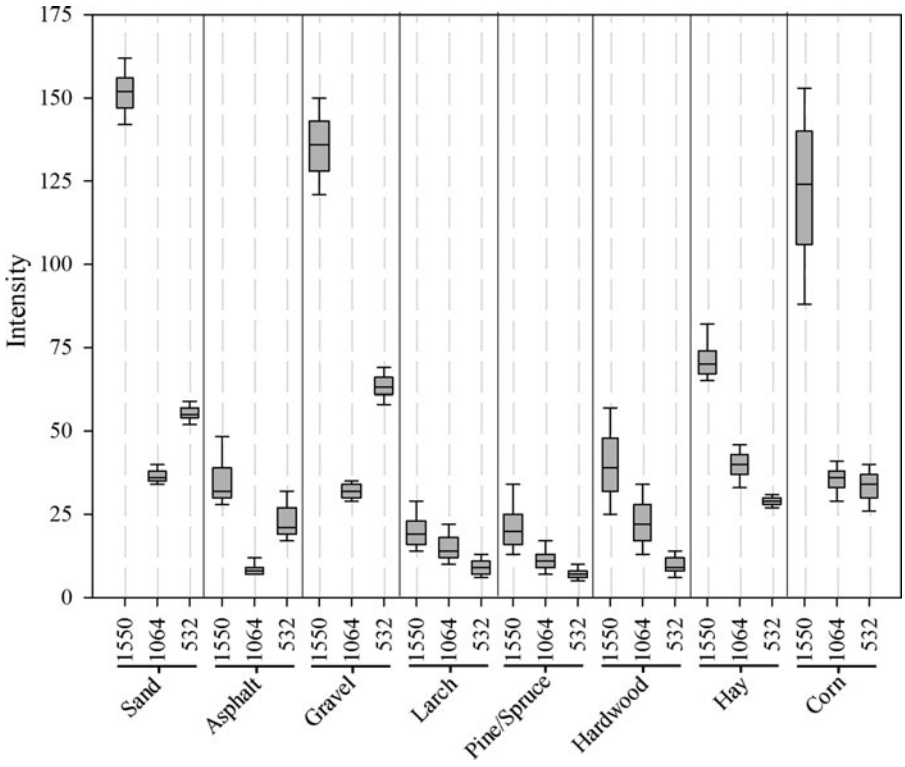

FIG. 9. Uncorrected intensity statistics for homogenous forest and land cover training sites identified in the field and using Google Earth. Error bars represent one standard deviation. (Note dominant hardwood is Maple [*Acer*]).

data possess less distinct wavelength-dependent deviations. It is likely, therefore, that although some of the percentile distribution attributes are controlled by the wavelength of the laser, the high deviations observed in the multisensor data have been amplified by other sensor and data collection influences. For example, the slight differences in survey altitude, FOV, sampling density, and flight line position could influence the canopy sampling geometry (Holmgren 2003; Hopkinson 2007) such as to compound any wavelength influences. Meanwhile, the primary elements of sampling geometry and density were kept constant across all 3 channels on the Titan and would, thus, be mitigated.

The similarity in overall trend indicates that the general sensor and wavelength behaviors of sampling upper or lower parts of the distribution (upper canopy vs. understory vs. ground) are characteristic of the wavelength and not the stand differences. However, the subtle differences in wavelength-dependent profile deviations among stand types indicate that each wavelength (or sampling configuration) provides a unique representation of the canopy, that when combined, helps differentiate stand type. The profile deviations constructed in Figure 8 can be considered analogous to signatures and, therefore, offer the potential for land cover classification. However, instead of being a 2D representation of spectral response, these profiles constitute a 3D

TABLE 5
2013 multisensor and 2015 single-sensor classification accuracy statistics

Mission	Classification	Average (%)	Overall (%)	Kappa
2013 (5 classes + null)	Minimum Distance	56.1	37.1	0.22
	Maximum Likelihood	77.2	69.8	0.59
	Parallelepiped (tie breaker)	74.5	64.0	0.53
2015 (8 classes + null)	Minimum Distance	77.6	78.0	0.74
	Maximum Likelihood	85.7	86.0	0.83
	Parallelepiped (tie breaker)	**87.3**	**87.9**	**0.85**

TABLE 6
2013 multisensor training site confusion matrix for 5 classes (plus null) using a maximum likelihood classification (column = actual; row = predicted); total training area used = 42,066 m^2

Class	Area (%)	Null	Conifer	Sand	Hardwood	Asphalt	Hay
Conifer	34	0.9	**64.8**	0	5.3	29.0	0
Sand	2	3.6	0	**93.2**	0	0	3.2
Hardwood	26	1.7	42.9	0	**43.0**	12.4	0
Asphalt	5	3.9	0.4	0.1	1.5	**94.0**	0.1
Hay	33	3.0	0	5.9	0.1	0	**90.9**

representation of canopy-depth-integrated response in 3 distinct bands.

Multispectral Classification

Thus far, the comparative evidence presented suggests that ground surface and forest canopy characteristics are uniquely represented at different LiDAR wavelengths. This is explicitly illustrated in Figure 9, where training site intensity summaries are illustrated for the 3e Titan wavelengths. Class separation using individual wavelength intensity thresholds is limited. At 1550 nm, larch would be inseparable from pine and spruce, and gravel would be inseparable from corn and sand. At 1064 nm alone, the same classes would be inseparable. However, the subtle differences in response between 1064 nm and 1550 nm, when combined with 532 nm, lead to distinct class signatures that offer the potential for multiband classification.

Training site accuracy statistics for each of the supervised classifications tested for 5 classes in 2013 and 8 classes in 2015 are presented in Table 5. Overall, the most successful 3-band intensity-based classification was the Titan data used to classify 8 land cover types with a parallelepiped routine (K = 0.85). Despite attempting to classify fewer land cover types, the 2013 multisensor results were less encouraging, with the best result returned from the maximum likelihood routine (K = 0.59).

The land cover types that were difficult to distinguish in the multisensor and Titan training datasets are evident in the associated confusion matrices (Tables 6 and 7, respectively). For the multisensor data, hardwood and conifer land cover types were the most difficult to distinguish, even though the training areas were known to be homogenous. There is even confusion between asphalt and the forested land cover types in the multisensor classification (Table 6), despite asphalt having a distinct response in the Titan datasets (Figure 9 and Table 7). For the Titan classification, 4 of the 8 classes produce >90% accuracy, with the lowest being larch at 65.8% (Table 7). Unsurprisingly, the main sources of confusion for the larch class are pine and spruce, then hardwood. Demonstrating that although classification of forest species using multispectral LiDAR shows promise, the overlap in the intensity channel responses might be too great for detailed or numerous classifications of specific forest species.

The final output of the Titan multispectral LiDAR intensity channel-based land cover classification is presented in Figure 10. Visual inspection of the image confirms that many of the land cover types are correctly classified, with roads, fields, bare sand, and gravel areas and the forest classes of larch, pine/spruce, and hardwood (primarily maple) conforming to their expected and known locations. The unclassified or null class tends to be associated with open canopy areas where understory shrub vegetation is prevalent or surrounding houses and farm

TABLE 7
2015 Titan training site confusion matrix for 8 classes (plus null) using a parallelepiped classification (column = actual; row = predicted); total training area used = 65,097 m^2

Class	Area (%)	Null	Corn	Gravel	Hay	Asphalt	Larch	Hardwood	Pine/Spruce	Sand
Corn	19	0.5	**94.3**	0	0.7	0.3	0	0.2	0	4.1
Gravel	3	0.4	0	**96.0**	0	0.3	0	0	0	3.3
Hay	20	0.1	1.5	0	**98.5**	0	0	0	0	0
Asphalt	10	1.8	0.3	0.9	0	**96.6**	0	0	0	0.3
Larch	4	0	0.2	0	0.1	0.2	**65.8**	4.1	29.6	0
Hardwood	23	0.7	0.4	0	0.1	0.6	7.7	**80.2**	10.5	0
Pine/Spruce	18	0.1	0.1	0	0	1.5	14.7	4.8	**78.9**	0
Sand	3	0	8.4	3.3	0	0.1	0	0	0	**88.2**

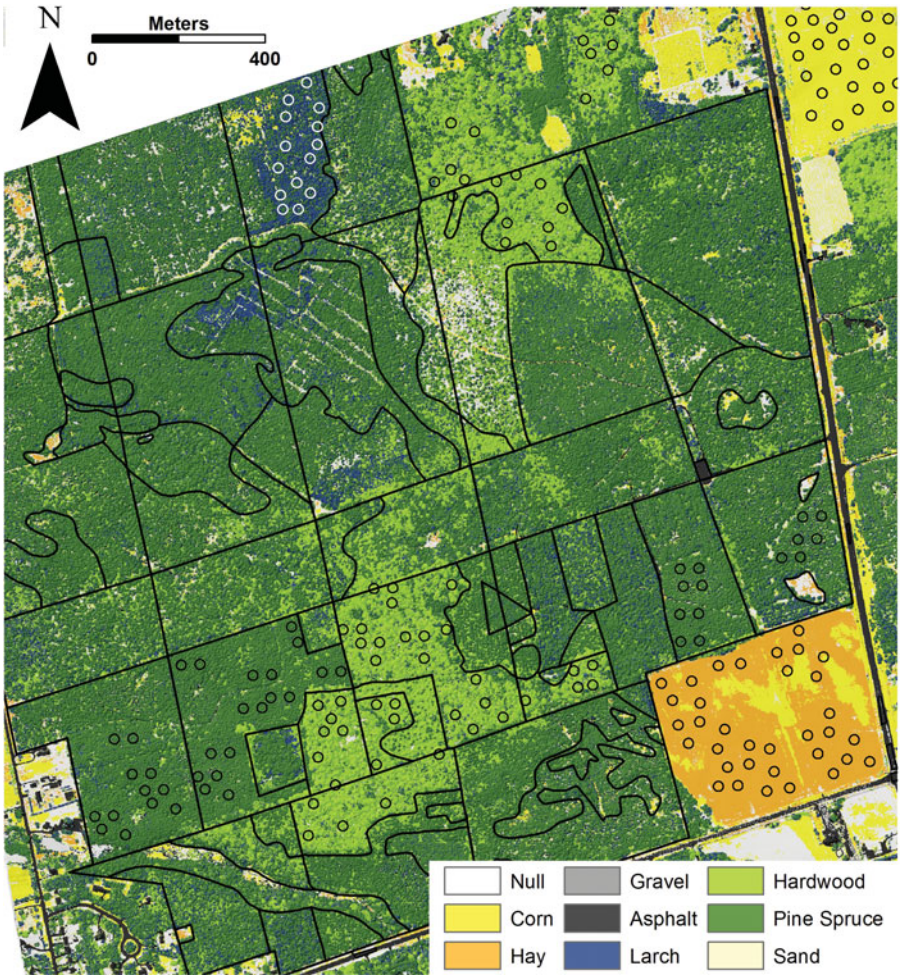

FIG. 10. Grid-level 1m resolution parallelepiped classification (with null class) of 8 dominant landcovers in the AOI for the 3-band composite 2015 Titan dataset. Training sites (circles) and FRI stand boundaries (black outlines) are illustrated.

buildings where gardens and urban infrastructure classes were not considered in training. One conspicuous misclassification is in the middle of the hay field in the SE corner of the AOI, where some areas are classified as corn. It is known from the field visit that the hay crop was patchy in places and it is possible that more of the unclassified soil signature is dominating these areas (see Figure 1) and creating the confusion with corn. Given this one clear example of misclassification, it is possible that similar

TABLE 8
2013 multisensor and 2015 single-sensor confusion matrices of FRI stands designated as either completely hardwood or conifer or nonforest compared against the proportion of stand area classified as hardwood, conifer, or any other (including null) landcover

FRI stand designation		MS LiDAR classified grid cells (%)		
		Hardwood	Conifer	Other
2013	Hardwood (n = 13)	25 (14)	48 (19)	27 (27)
	Conifer (n = 41)	10 (12)	51 (26)	39 (30)
	Nonforest (n = 6)	16 (17)	28 (30)	56 (36)
2015	Hardwood (n = 13)	52 (27)	41 (24)	7 (10)
	Conifer (n = 51)	16 (15)	79 (15)	5 (5)
	Nonforest (n = 8)	9 (7)	43 (27)	48 (31)

Standard deviation in brackets.

TABLE 9
Plot-level proportions of hardwood vs. conifer basal area (BA) measured in the field and the corresponding differences in areal proportions of classified hardwood (HW) vs. conifer; other class means grid cells were neither hardwood or conifer

			Class Proportion Differences from Field BA (%)					
	BA field Proportion (%)		2013 Multisensor			2015 Single-Sensor		
Plot	Conifer	HW	Conifer	HW	Other	Conifer	HW	Other
1	0	100	42	−47	5	24	−25	1
2	0	100	57	−66	10	19	−19	0
3	75	25	−2	−18	20	3	−3	0
4	80	20	−3	−9	12	−3	3	0
5	99	1	−19	5	14	−7	6	0
6	91	9	−23	0	23	3	−4	1
7	100	0	−25	1	24	−1	1	0
8	0	100	57	−67	10	23	−23	0
Avg(SD)	**56(47)**	**44(47)**	**11(36)**	**−25(30)**	**15(7)**	**8(12)**	**−8 (13)**	**0(0)**

errors have occurred over the forest stands where it would be less obvious.

A confusion matrix of FRI stands designated as entirely hardwood or conifer or nonforest cover, vs. the proportion of 1-m cells classified as hardwood or conifer (pine, spruce, or larch) is presented in Table 8. For the 2015 hardwood FRI stands, the majority of the area (52%) was classified as hardwood, whereas in conifer stands, the area classified as conifer was 79%, and in nonforest covered stands, 43% were classified as something other than forest. In each stand designation, the dominant areal Titan classifications were in general agreement. Complete agreement was not expected, because all stands contain trees outside the FRI designation class, and where the ground surface is visible in the 1-m LiDAR classification, the area is frequently classified as null or some other nonforest land cover (Figure 10). The results for the multisensor classification were poor by comparison with increased confusion throughout the classes. The nonforest class was more correctly identified in the multisensor data (56%) vs the Titan data (48%), however, due to fewer land cover types in 2013, 52% of the image was unclassified, whereas for 2015, only 24% of the image remained unclassified. Consequently, the nonforest class was >2 times more likely in the 2013 vs. 2015 classification, and this result should not be taken to suggest the multisensor data are better able to classify nonforest areas than the Titan.

FRI stand designations are coarse, however, and not completely representative of the species mix and proportions in an individual stand. In the field, it was not possible to easily and accurately map the upper crown surface extent for each tree, so plot-level basal area was used as an index of hardwood vs, conifer areal proportion. For each of the 8 closed-canopy plots visited, the basal area proportions are presented alongside the associated areal classification proportions of hardwood and conifer (Table 9). 50% of the plots were either entirely conifer or hardwood, with the remainder being mixed. There is limited correspondence for the 2013 classes, with mean discrepancies of $+11\%$ and -25% for conifer and hardwood, respectively. The mean discrepancies for the 2015 plot data are $+8\%$ and -8%, respectively. Of note, however, is that for 2015, no other classes are present in these plot areas and the residuals are small compared to those of 2013 (Table 9).

CONCLUSIONS

From DEM, P99, percentile and gap probability comparisons performed using both multisensor and single-sensor multispectral LiDAR data, it has been shown that forest environment characterization differs with laser wavelength. For the comparison of individual sensors, this observation has potentially negative implications for either long-term monitoring or large area integration of LiDAR data from a range of sources. Differences in terrain and canopy representation from different sensors has 3 consequences: (*i*) the transferability of models across datasets will be limited; (*ii*) training data will be required for data derived from different sensors; (*iii*) if models are widely applied, users should expect higher levels of uncertainty and bias, which will vary by data source.

However, it has also been demonstrated that when sampling configuration inconsistencies associated with different sensors and platforms are removed by integration of multiple lasers into a single sensor, systematic wavelength-dependent differences still occur but are more subtle. Canopy profile differences between wavelengths and stand types are minor at ground and canopy top, but are pronounced at low- to mid-height percentiles and when modeling gap probability from return ratios. The light penetration, absorption, and reflection characteristics vary such that the returns from each wavelength do not sample the same parts of the foliage profile. This is likely at least partially influenced by profile variation in leafy vs, woody proportions and

the different relative reflectance properties in each wavelength (Korpela et al. 2010). Studies combining optical and LiDAR data have attempted similar canopy structural separations, but this is traditionally challenging due to uncertainty in the 3D source of the optical response within a canopy (e.g., Niemann et al. 2012). The active multispectral observations presented here suggest that there is potential for separation of woody and leafy foliage within the canopy, using the relative proportions of wavelength response at each height interval, but this remains to be tested.

Although airborne LiDAR canopy foliage profile classification remains elusive, differences in planimetric land surface reflectance in each active laser wavelength can be used to support high-resolution land surface classification. This was demonstrated by using the 3 Titan intensity channels alone to classify 8 distinct land cover types ($K = 0.85$). The multisensor classification over the same area, using intensity data alone, was able to classify 5 land cover types at lower accuracy ($K = 0.53$). Within the single-intensity channels of any sensor, the overlap in intensity values between land cover types is sufficiently high to prevent accurate classification of even 5 of the dominant land cover types in the AOI.

Land cover classification using LiDAR derivatives, including intensity, is becoming main stream. In addition, the classification presented in Figure 10 is unimpressive compared to what is possible using high-resolution multispectral data. However, using LiDAR intensity alone to classify multiple land cover types with acceptable accuracy has previously not been demonstrated for land surfaces with similar characteristics. Therefore, the simple 8 land cover classifications presented as an example here, constitute a minimal level of capability for single sensor multispectral LiDAR. Similar image-based supervised classifications will be aided significantly through the inclusion of terrain and canopy structural metrics derived from the point cloud. Further enhancements will follow from the inclusion of supplemental data sources such as coincident optical imagery, or the utilization of more sophisticated classification routines (Holmgren et al. 2008; Vaukonen et al. 2010).

The intensity data produced from the LiDAR sensors in this study could not be radiometrically corrected, due to there being no coincident ground reflectance data available for channel calibrations. Also, due to the proprietary nature of the hardware design and intensity recording procedure, there was insufficient data to physically calculate the radiometric response of each sensor's receiver channel. Consequently, the ability to accurately ratio wavelengths to derive vegetation indices is currently limited and was not evaluated. With ground reflectance target data (Kaasalainen et al. 2009), however, this could be achieved and so is a logical next step in land cover or vegetation species classification.

ACKNOWLEDGMENTS

Teledyne Optech is gratefully acknowledged for flying the airborne missions and supplying the LiDAR data. Zhouxin Xi, and Ron and Pam Chasmer are acknowledged for providing field support.

FUNDING

Hopkinson acknowledges Discovery Grant funding through the Natural Sciences and Engineering Research Council; equipment funding through the Canada Foundation for Innovation and Laboratory funding through Campus Alberta. Chasmer acknowledges funding from Alberta Innovates Technology Futures.

REFERENCES

Antonarakis, A.S., Richards, K.S., and Brasington, J. 2008. "Object-based land cover classification using airborne LiDAR." *Remote Sensing of Environment*, Vol. 112: pp. 2988–2998.

Axelsson, P. 1999. "Processing of laser scanner data - algorithms and applications." *ISPRS Journal of Photogrammetry and Remote Sensing*, Vol. 54: pp. 138–147.

Chasmer, L.E., Hopkinson, C., and Treitz, P. 2006. "Investigating laser pulse penetration through a conifer canopy by integrating airborne and terrestrial LiDAR." *Canadian Journal of Remote Sensing*, Vol. 32(No. 2): pp. 116–125.

Clark, M.L., Clark, D.B., and Roberts, D.A. 2004. "Small-footprint LiDAR estimation of sub-canopy elevation and tree height in a tropical rain forest landscape." *Remote Sensing of Environment*, Vol. 91(No. 1): pp. 68–89.

Colwell, J.E. 1974. "Vegetation canopy reflectance." *Remote Sensing of Environment*, Vol. 3(No. 3): pp. 175–183.

Crasto, N., Hopkinson, C., Marsh, P., Forbes, D., Lesack, L., and Spooner, I. 2015. "Open-water classification in the Mackenzie Delta, NWT using airborne LIDAR." *Remote Sensing of Environment*, Vol. 164: pp. 90–102.

Dubayah, R.O., and Drake, J.B. 2000. "LiDAR remote sensing for forestry." *Journal of Forestry*, Vol. 98(No. 6): pp. 44–46.

Elberink, S.O., Stoter, J., Ledoux, H., and Commandeur, T. 2013. "Generation and dissemination of a national virtual 3D city and landscape model for the Netherlands." *Photogrammetric Engineering and Remote Sensing*, Vol. 79(No. 2): pp. 147–158

Gates, D.M. 1970. "Physical and physiological properties of plants." In *Remote Sensing with Special Reference to Agriculture and Forestry*, pp. 224–252. Washington, DC, USA: National Academy of Sciences.

Goetz, A.F.H., Rock, B.N., and Rowan, L.C. 1983. "Remote-sensing for exploration - an overview." *Economic Geology*, Vol. 78(No. 4): pp. 573–590.

Goodale, R., Hopkinson, C., Colville, D., and Amirault. D. 2007. "Mapping Piping Plover habitat in coastal areas using airborne LiDAR data." *Canadian Journal of Remote Sensing*, Vol. 33(No. 6): pp. 519–533.

Hancock, S., Lewis, P., Foster, M., Disney, M., and Muller, J.P. 2012. "Measuring forests with dual wavelength LiDAR: A simulation study over topography." *Agricultural and Forest Meteorology*, Vol. 161: pp. 123–133.

Hogg, A.R., and Todd, K.W. 2007. "Automated discrimination of upland and wetland using terrain derivatives." *Canadian Journal of Remote Sensing*, Vol. 33(No. S1): pp. S68–S83.

Holmgren, J., Nilsson, M., and Olsson, H. 2003. "Simulating the effects of LiDAR scanning angle for estimation of mean tree height and

canopy closure." *Canadian Journal of Remote Sensing*, Vol. 29(No. 5): pp. 623–632.

Holmgren, J., Persson, Å., and Söderman, U. 2008. "Species identification of individual trees by combining high resolution LiDAR data with multispectral images." *International Journal of Remote Sensing*, Vol. 29: pp. 1537–1552.

Hopkinson, C. 2007. "The influence of flying altitude and beam divergence on canopy penetration and laser pulse return distribution characteristics." *Canadian Journal of Remote Sensing*, Vol. 33(No. 4): pp. 312–324.

Hopkinson, C., and Chasmer, L. 2009. "Testing LiDAR models of fractional cover across multiple forest ecozones."*Remote Sensing of Environment*, Vol. 113(No. 1): pp. 275–288.

Hopkinson, C., Chasmer, L.E., Hall, R.J. 2008. "The uncertainty in conifer plantation growth prediction from multitemporal LiDAR datasets." *Remote Sensing of Environment*, Vol. 112(No. 3): pp. 1168–1180.

Hopkinson, C., Chasmer, L.E., Young-Pow, C., and Treitz, P. 2004. "Assessing plot-level forest metrics with a ground-based scanning LiDAR." *Canadian Journal of Forest Research*, Vol. 34: pp. 573–583.

Hopkinson, C., Colville, D., Bourdeau, D., Monette, S., and Maher, R. 2011. "Scaling plot to stand-level LiDAR to public GIS data in a hierarchical approach to map the biomass of Nova Scotia." Paper presented at Proceedings of the SilviLaser 2011 Conference, Hobart, Tasmania, Oct. 16–20. Unpaginated USB.

Irish, J.L., and Lillycrop, W.J. 1999. "Scanning laser mapping of the coastal zone: the SHOALS system." *ISPRS Journal of Photogrammetry & Remote Sensing*. Vol. 54: pp. 123–129

Kaasalainen, S., Hyyppä, H., Kukko, A., Ahokas, E., Hyyppä, J., Lehner, H., Jaakkola, et al. 2009. "Radiometric calibration of LIDAR intensity with commercially available reference targets." *IEEE Transactions on Geoscience and Remote Sensing*, Vol. 47(No. 2): pp. 588–499

Ke, Y., Quackenbush, L.J., and Im, J. 2010. "Synergistic use of QuickBird multispectral imagery and LIDAR data for object-based forest species classification." *Remote Sensing of Environment*, Vol. 114: pp. 1141–1154.

Knipling, E.B. 1970. "Physical and physiological basis for the reflectance of visible and near-infrared radiation from vegetation." *Remote Sensing of Environment*, Vol. 1(No. 3): pp. 155–159.

Korpela, I., Ørka, H.O., Maltamo, M., Tolola, T., and Hyyppä, J. 2010. "Tree species classification using airborne LiDAR – effects of stand and tree parameters, downsizing of training set, intensity normalization, and sensor type." *Silva Fennica*, Vol. 44(No. 2): pp. 319–339.

Koukoulas, S., and Blackburn, G.A. 2005. "Mapping individual tree location, height and species in broadleaved deciduous forest using airborne LIDAR and multispectral remotely sensed data." *International Journal of Remote Sensing*, Vol. 26(No. 3): pp. 431–455.

Lefsky, M.A., Harding, D., Cohen, W.B., Parker, G., and Shugart, H.H. 1999. "Surface LiDAR remote sensing of basal area and biomass in deciduous forests of eastern Maryland, USA." *Remote Sensing of Environment*, Vol. 67(No. 1): pp. 83–98.

Lefsky, M.A., Cohen, W.B., Parker, G.G., and Harding, D.J. 2002. "LiDAR remote sensing for ecosystem studies." *Bioscience*, Vol. 52(No. 1): pp. 19–30.

Lim, K., Hopkinson, C., and Treitz, P. 2008. "Examining the effects of sampling point densities on laser canopy height and density metrics at the forest plot level." *Forestry Chronicle*, Vol. 84(No. 6): pp. 876–885

Lobell, D.B., and Asner, G.P. 2002. "Moisture effects on soil reflectance." *Soil Science Society of America Journal*, Vol. 66(No. 3): pp. 722–727.

McRoberts, R.E., Næsset, E., Gobakken, T., and Bollandsås, O.M. 2015. "Indirect and direct estimation of forest biomass change using forest inventory and airborne laser scanning data." *Remote Sensing of Environment*, Vol. 164: pp. 36–42.

Means, J.E., Acker, S.A., Fitt, B.J., Renslow, M., Emerson, L., and Hendrix, C.J. 2000. "Predicting forest stand characteristics with airborne scanning LiDAR." *Photogrammetric Engineering and Remote Sensing*, Vol. 66(No. 11): pp. 1367–1371.

Means, J.E., Acker, S.A., Harding, D.J., Blair, J.B., Lefsky, M.A., Cohen, W.B., Harmon, M.E., and McKee, W.A. 1999. "Use of large-footprint scanning airborne LiDAR to estimate forest stand characteristics in the Western Cascades of Oregon." *Remote Sensing of Environment*, Vol. 67(No. 3): pp. 298–308.

Millard, K., and Richardson, M. 2013. "Wetland mapping with LiDAR derivatives, SAR polarimetric decompositions, and LiDAR–SAR fusion using a random forest classifier." *Canadian Journal of Remote Sensing*, Vol. 39(No. 4): pp. 290–307.

Moffiet, T., Mengersen, K., Witte, C., King, R., and Denham, R. 2005. "Airborne laser scanning: Exploratory data analysis indicates potential variables for classification of individual trees or forest stands according to species." *ISPRS Journal of Photogrammetry and Remote Sensing*, Vol. 59(No. 5): pp. 289–309.

Montaghi, A. 2013. "Effect of scanning angle on vegetation metrics derived from a nationwide airborne laser scanning acquisition." *Canadian Journal of Remote Sensing*, Vol. 39(No. s1): pp. S152–S173.

Morsdorf, F., Nichol, C., Malthus, T., and Woodhouse, I.H. 2009. "Assessing forest structural and physiological information content of multispectral LiDAR waveforms by radiative transfer modelling." *Remote Sensing of Environment*, Vol. 113(No. 10): pp. 2152–2163.

Næsset, E. 2009. "Effects of different sensors, flying altitudes, and pulse repetition frequencies on forest canopy metrics and biophysical stand properties derived from small-footprint airborne laser data." *Remote Sensing of Environment*, Vol. 113 (No. 1): pp. 148–159

Naesset, E., 2002. "Predicting forest stand characteristics with airborne scanning laser using a practical two-stage procedure and field data." *Remote Sensing of Environment*, Vol. 80(No. 1): pp. 88–99.

Nelson, R. 2013. "How did we get here? An early history of forestry LiDAR." *Canadian Journal of Remote Sensing*, Vol. 39(No. s1): pp. S6–S17.

Nelson, R., Krabill, W., and Maclean, G. 1984. "Determining forest canopy characteristics using airborne laser data." *Remote Sensing of Environment*, Vol. 15(No. 3): pp. 201–212.

Niemann, K.O., Quinn, G., Goodenough, D.G., Visintini, F., and Loos, R. 2012. "Addressing the effects of canopy structure on the remote sensing of foliar chemistry of a 3-dimensional, radiometrically porous surface." *IEEE Journal of Selected Topics in Applied Earth Observations and Remote Sensing*, Vol. 5(No. 2): pp. 584–593.

Ni-Meister, W., Lee, S.Y., Strahler, A.H., Woodcock, C.E., Schaaf, C., Yao,T.A., Ranson, K.J., Sun G.Q., and Blair, J.B. 2010. "Assessing general relationships between aboveground biomass and vegetation

structure parameters for improved carbon estimate from LiDAR remote sensing." *Journal of Geophysical Research-Biogeosciences*, Vol. 115. doi: 10.1029/2009JG000936

Ørka, H.O., Næsset, E., and Bollandsås, O.M. 2007. "Utilizing airborne laser intensity for tree species classification." *International Archives of the Photogrammetry, Remote Sensing and Spatial Information Sciences*, Vol. 36(No. 3/W52): pp. 300–304.

Ørka, H.O., Næsset, E., and Bollandsås, O.M. 2009. "Classifying species of individual trees by intensity and structure features derived from airborne laser scanner data." *Remote Sensing of Environment*, Vol. 113(No. 6): pp. 1163–1174.

Patenaude, G., Hill, R.A., Milne, R., Gaveau, D.L.A., Briggs, B.B.J., and Dawson, T.P. 2004. "Quantifying forest above ground carbon content using LiDAR remote sensing." *Remote Sensing of Environment*, Vol. 93(No. 3): pp. 368–380.

Rosette, J., Suarez, J., North, P., and Los, S. 2011. "Forestry applications for satellite LiDAR remote sensing." *Photogrammetric Engineering and Remote Sensing*, Vol. 77(No. 3): pp. 271–279.

Satterwhite, M.B., and Henley, J.P. 1990. *Hyperspectral Signatures (400 to 2500 nm) of Vegetation, Minerals, Soils, Rocks, and Cultural Features: Laboratory and Field Measurements. DTIC Document*. Fort Belvoir, VA. Army Engineer Topographic Labs.

Stoker, J.M., Cochrane, M.A., Roy, D.P. 2014. "Integrating disparate Lidar data at the national scale to assess the relationships between height above ground, land cover and ecoregions." *Photogrammetric Engineering and Remote Sensing*, Vol. 80(No. 1): pp. 59–70.

St-Onge, B., Hu, Y., and Véga, C. 2008. "Mapping the height and above-ground biomass of a mixed forest using LiDAR and stereo Ikonos images." *International Journal of Remote Sensing.* Vol. 29(No. 5): pp. 1277–1294.

St-Onge, B., Jumelet, J., Cobello, M., and Véga, C. 2004. "Measuring individual tree height using a combination of stereophotogrammetry and LiDAR." *Canadian Journal of Forest Research*, Vol. 34(No. 10): pp. 2122–2130.

Vauhkonen, J., Korpela, I., Maltamo, M., Tokola, T. 2010. "Imputation of single-tree attributes using airborne laser scanning-based height, intensity, and alpha shape metrics." *Remote Sesning of Environment*, Vol. 114: pp. 1263–1276.

Wallace, A., Nichol, C., and Woodhouse, I. 2012. "Recovery of forest canopy parameters by inversion of multispectral LiDAR data." *Remote Sensing*, Vol. 4(No. 2): pp. 509–531.

Woodhouse, I.H., Nichol, C., Sinclair, P., Jack, J., Morsdorf, F., Malthus, T.J., and Patenaude, G. 2011. "A multispectral canopy LiDAR demonstrator project." *IEEE Geoscience and Remote Sensing Letters*, Vol. 8: pp. 839–843. doi: 10.1109/Lgrs.2011.2113312.

Woods, M., Pitt, D., Penner, M., Lim, K., Nesbitt, D., Etheridge, D., and Treitz, P. 2011. "Operational implementation of a LiDAR inventory in Boreal Ontario." *The Forestry Chronicle*, Vol. 87(No. 4): pp. 512–528.

Wulder, M.A., White, J.C., Bater, C.W., Coops, N.C., Hopkinson, C., and Chen, G. 2012. "LiDAR plots-a new large-area data collection option: context, concepts, and case study." *Canadian Journal of Remote Sensing*, Vol. 38(No. 5): pp. 600–618.

Yan, W.Y., Shaker, A. and El-Ashmawy, N. 2015. "Urban land cover classification using airborne LiDAR data: A review." *Remote Sensing of Environment*, Vol. 158: pp. 295–310.

Yan, W.Y., and Shaker, A. 2015. "Radiometric normalization of overlapping LiDAR intensity data for reduction of line striping noise." *International Journal of Digital Earth*. (Submitted).

Yang, X., Rochdi, N., Zhang, J., Banting, J., Rolfson, D., King, C., Staenz, K., Patterson, S., and Purdy, B. 2014. "Mapping tree species in a boreal forest area using RapidEye and LIDAR data." In *Proceedings of the IEEE International Geoscience and Remote Sensing Society conference*. IEEE.

Yu, X., Hyyppä J., Kaartinen H., and Maltamo M. 2004. "Automatic detection of harvested trees and determination of forest growth using airborne laser scanning." *Remote Sensing of Environment*, Vol. 90(No. 4): pp. 451–462.